Comparing heterogeneity of sea ice models with Viscous-Plastic and Maxwell Elasto-Brittle rheology

Mirjam BOURGETT[1], Martin LOSCH[1], Mathieu PLANTE[2]

[1] *Alfred-Wegener-Institut für Polar- und Meeresforschung, Bremerhaven, Germany*

[2] *Recherche en prévision numérique environnementale, Environnement et Changement Climatique Canada, Dorval, Québec, Canada*

Correspondence: Mirjam Bourgett <mirjam.bourgett@awi.de>

ABSTRACT.

Classical sea-ice models in climate model resolution do not resolve the small scale physics of sea ice. New methods to address this problem include modifications to established viscous-plastic (VP) rheology models, sub-grid scale parameterisations, or new rheologies such as the Maxwell elasto-brittle (MEB) rheology. Here, we investigate differences in grid-scale dynamics simulated by the VP and MEB models, their dependency on tunable model parameters and their response to added stochastic pertubations of material patameters in a new implementation in the Massachusetts Institute of Technology general circulation model. Idealized simulations are used to demonstrate that material parameters can be tuned so that both VP and MEB rheologies lead to similar cohesive stress states, arching behavior, and hetereogeneity in the deformation fields. As expected, simulations with MEB rheology generally show more heterogeneity than the VP model as measured by the number of simulated linear kinematic features (LKFs). For both rheologies, the cohesion determines the emergence of LKFs. Introducing grid-scale heterogeneity by random model parameter perturbation, however, leads to a larger increase of LKF numbers in the VP simulations than in the MEB simulations and similar heterogeneity between VP and MEB models.

INTRODUCTION

Representing sea ice deformations in large scale climate models is important but challenging as the large scale sea ice conditions very much depend on smaller-scale physics that are poorly resolved at coarse resolution. Most continuum sea ice models use the viscous-plastic (VP) rheology (Hibler, 1979) or modifications (e.g. the Elastic Viscous Plastic or EVP, Hunke and Dukowicz, 1997), which has been used for decades to reproduce the observed sea ice thickness, concentration and velocity fields. At high resolution, VP models are able to reproduce some of the large scale statistics of sea ice deformations, for instance the observed multi-fractal spatial and temporal scaling (Hutter and Losch, 2020; Bouchat and others, 2022; Hutter and others, 2022). At coarser resolutions, however, the scaling properties of sea ice deformations from VP models can be inconsistent with observations (Weiss and others, 2007; Bouchat and others, 2022; Hutter and others, 2022). In particular, models using the VP rheology tend to underestimate intermittency and spatial heterogeneity because they cannot trigger multi-scale deformation events from smaller scale perturbations (Weiss and others, 2007). At grid resolutions of ≈12 km, the VP rheology did not reproduce the complicated fracturing processes associated with sea ice deformations and their organisation into a network of localised lines with large deformations called Linear Kinematic Features (LKFs) (Girard and others, 2011).

This challenge sparked different approaches to include smaller scale characteristics in large scale models. To allow for fine scale features, existing VP models were modified to use different yield curves (Ringeisen and others, 2019, 2023), flow rules (Ringeisen and others, 2021), grids (Danilov and others, 2017; Turner and others, 2022; Rampal and others, 2016) and numerical methods (Lemieux and others, 2008, 2010; Losch and others, 2014). Alternatively, new rheologies were suggested that include sub-grid parameterisations to better represent fracture physics. In particular, brittle (elasto-brittle or EB, Maxwell elasto-brittle or MEB, brittle Bingham-Maxwell or BBM) rheologies (Girard and others, 2011; Dansereau and others, 2016; Olason and others, 2022) introduced a damage parameter that represents the presence of sub-grid scale fractures, allowing for (and keeping a memory of) material property degradation under high stresses without large deformations. These still relatively new brittle rheologies simulate realistic large scale fields with adequate heterogeneity and intermittency even at coarser resolution (grid spacing of ≈10 km) (e.g Olason and others, 2022). Another way of accounting for the missing physical sub-grid scale processes is to use stochastic parameterizations (e.g. Juricke and others, 2013) where the effect of unresolved small scales on the large scales are not modeled in a deterministic way from the resolved flow, but by randomly perturbing selected model parameters (Berner and others, 2017). This method has also been used with brittle rheologies in idealized experiments (Girard and others, 2011; Dansereau and others, 2016).

As part of their development, new rheology parameterizations are often evaluated in idealised experiments that are designed to test, tune, and compare the model to observed sea ice dynamical behaviour. For instance, ideal ice bridge experiments have been used with both the (E)VP (e.g., Dumont and others, 2009; Losch and Danilov, 2012) and MEB (e.g., Dansereau and others, 2017; Plante and others, 2020) rheologies to demonstrate their ability to reproduce the observed tendency for sea ice flow to become obstructed by the formation of self-supporting ice arches in narrow channels (Walker, 1966; Sodhi, 1977). Uniaxial compression experiments have been used to assess the influence of the plastic flow rules on the orientation of LKFs in VP models (Ringeisen and others, 2019, 2021, 2023). A benchmark experiment was also designed to assess the LKFs and heterogeneity in the sea ice cover under convergent or divergent wind forcing. This benchmark experiment proved useful to formulate metrics and compare LKFs statistics from different sea ice models (Mehlmann and others, 2021; Hutter and Losch, 2020).

Often a given sea ice model code implements only one type of rheology. This leads to rheology comparisons that are confounded by numerical discretization, advection scheme, and grid resolution (Bouchat and others, 2022; Hutter and others, 2022). Sea ice model codes that contain more than one rheology are, for example, the McGill sea ice model (Plante and others, 2020) or the neXtSIM (Olason and others, 2022). The McGill model contains the MEB and an implicit VP rheology with different solution techniques, but is not coupled to an ocean (Plante and others, 2020). The neXtSIM framework, for which coupled set-ups exist, is a Langrangian sea ice model and implements MEB, BBM, and m(odified)EVP rheology (Olason and others, 2022; Boutin and others, 2023). Here, we add the MEB rheology to the sea ice component (Losch and others, 2010) of the open source Massachusetts Institute of Technology general circulation model (MITgcm, Marshall and others, 1997; MITgcm Group, 2021). The sea ice component already contains VP rheologies with many different options and yield curves (Losch and others, 2010, 2014; Kimmritz and others, 2016; Ringeisen and others, 2023; MITgcm Group, 2021) for the purpose of unconfounded comparisons between sea ice rheologies in a coupled ice ocean framework.

In this paper, we investigate the sea ice deformations and heterogeneity simulated by the VP and MEB rheologies in the context of ideal ice bridge and benchmark experiments. To do so, the MEB rheology is implemented in the MITgcm sea ice component as to provide an unconfounded comparison framework.

The MEB implementation follows and is validated against Plante and others (2020). A similar ice bridge experiment is then used to compare deformation features of simulations with MEB and VP rheology. The spatial heterogeneity simulated with both rheologies is then evaluated in an idealized quadratic domain with cyclonic winds (Mehlmann and others, 2021) by tracking LKFs. To further increase spatial heterogeneity with both VP and MEB rheologies a stochastic parameterisation is presented.

MODEL DESCRIPTION

The MITgcm is a general circulation model used to study atmosphere, ocean, and climate processes at all scales (Marshall and others, 1997; MITgcm Group, 2021). It employs a finite volume discretization on an Arakawa C-grid. The sea ice model is coupled to the ocean and implements the VP rheology (Hibler, 1979) with a number of yield curves and solvers (e.g., Losch and others, 2010, 2014; Kimmritz and others, 2016; Ringeisen and others, 2023; MITgcm Group, 2021). The MITgcm model code and documentation can be found at `https://mitgcm.org`. This paper addresses the dynamics of the sea ice model and all thermodynamics processes are turned off.

MEB constitutive equation

The MEB rheology consists of a linear elastic part of the constitutive equation for a continuous solid, a viscous part of the constitutive equation for irreversible deformations, a local Mohr Coulomb (MC) criterion for brittle failure, and an isotropic progressive damage mechanism that rescales the viscous and elastic dynamics to initiate avalanches of damage (Dansereau and others, 2016). We repeat the main aspects here for clarity.

The constitutive equation for vertically integrated internal stress $\boldsymbol{\sigma}$ (here in $\mathrm{Pa\,m} = \mathrm{N\,m^{-1}}$) and strain rates $\dot{\boldsymbol{\varepsilon}}$ for a 2D compressible, visco-elastic, continuous solid is

$$\dot{\boldsymbol{\sigma}} + \lambda^{-1}\boldsymbol{\sigma} = E(d)\,\boldsymbol{C} \cdot \dot{\boldsymbol{\varepsilon}} \tag{1}$$

with the elastic modulus tensor $\boldsymbol{C}$ (a function of the Poisson ratio ν) and the viscous relaxation time scale λ. Note that the stress and strain rate tensors are reduced in their order by using the Voigt notation for symmetric tensors. The relaxation time scale λ is written as the ratio of the viscosity ξ, the elastic modulus E, and a damage parameter d representing the amount material degradation from accumulating micro (sub-grid) cracks in the sea ice (Dansereau and others, 2016):

$$\lambda = \frac{\xi(d)}{E(d)} = \lambda_0 \, (1 - d)^{\alpha - 1} \tag{2}$$

where ξ and E depend on the fractional ice cover, mean ice thickness (i.e., using the forumulation for the VP ice strength of Hibler, 1979) and $\alpha > 1$ is a parameter ruling the transition from elastic to viscous behaviour. E_0 and ξ_0 are the undamaged mechanical parameters and $\lambda_0 = \frac{\xi_0}{E_0}$. In contrast to some previous work (e.g., Dansereau and others, 2016), we define damage so that $d = 0$ for undamaged ice and $d = 1$ for maximally damaged ice.

The damage increases when the stress states exceed the yield curve (Fig. 1) and it contains the history of the previous damaging events (Dansereau and others, 2016; Plante and others, 2020). The increase depends on the scaling factor d_{crit} (critical damage, which is determined by the requirement to bring the overshooting stress state back to the yield curve).

One possible yield curve for the MEB rheology is the MC criterion with a tensile cut-off (Fig. 1) (Dansereau and others, 2016). The critical uniaxial compressive stress σ_c at the intersection of the MC yield curve with the principal stress σ_1 axis (Fig. 1) is

$$\sigma_c = 2\, ch\sqrt{q} \tag{3}$$

where c is the cohesion and $q = \left((\mu^2 + 1)^{1/2} + \mu\right)^2$ is the slope defined by the internal friction coefficient μ. In contrast to the standard elliptic yield curve of a VP rheology (Hibler, 1979), this yield curve permits isotropic tensile stresses. The critical tensile stress σ_t is defined as the intersection of the principal stress σ_2 axis with the MC criterion (Fig. 1) so that

$$\sigma_t = -\frac{\sigma_c}{q}. \tag{4}$$

Implementation details

The finite-volume implementation on the C-grid of the MITgcm sea ice model follows for the most part the implementation of the MEB rheology in the finite-differences C-grid implementation in the McGill sea ice model (Plante and others, 2020).

We note the structural similarity of the MEB and VP constitutive equations: the product of the elastic

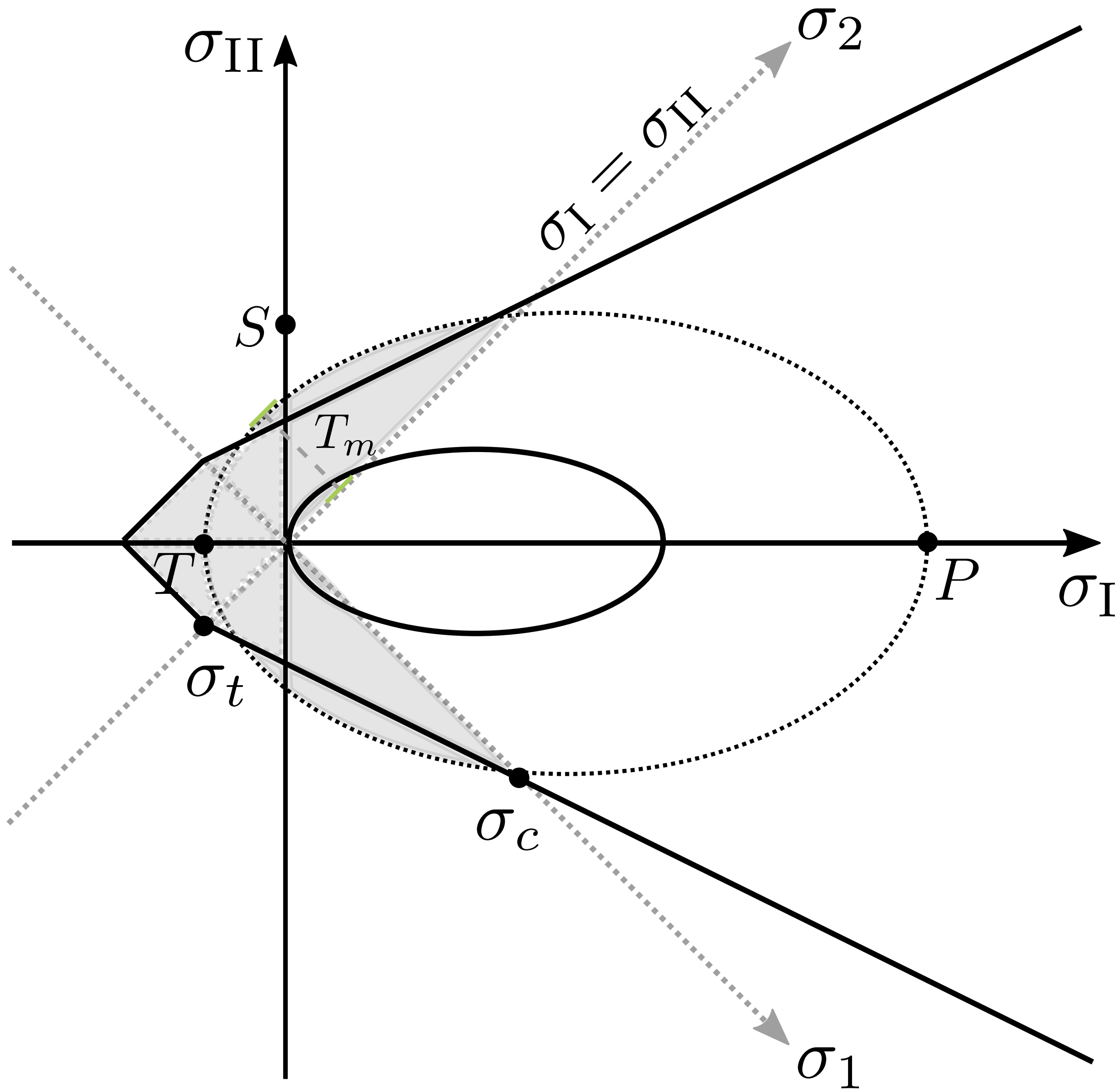

Fig. 1. Illustration of elliptic yield curve (VP, black dotted and solid ellipses) and Mohr-Coulomb yield curve (MEB, black piecewise linear lines). Invariant stress axes (σ_I, σ_{II}) in black and principal stress axes (σ_1, σ_2) in grey. σ_c is the critical uniaxial compressive stress (Eq. 3) and σ_t is the critical tensile stress (Eq. 4). The maximum tensile stress T_m (Eq. 6) is indicated by the green dashed line. a and b denote the semi-major axes of the elliptic yield curve. Grey shading marks the cohesive stress states.

modulus tensor $\boldsymbol{C}$ and the strain rate tensor $\dot{\boldsymbol{\varepsilon}}$ in (1) is (e.g., Dansereau and others, 2016)

$$[\boldsymbol{C} \cdot \dot{\boldsymbol{\varepsilon}}^n]_{ij} = \frac{\nu}{(1+\nu)(1-\nu)} \dot{\varepsilon}_{kk}\delta_{ij} + \frac{1}{1+\nu}\dot{\varepsilon}_{ij}. \tag{5}$$

This is the same form as the VP constitutive equation $\sigma_{ij} = 2\eta\dot{\varepsilon}_{ij} + \left[(\zeta - \eta)\dot{\varepsilon}_{kk} - \frac{P}{2}\right]\delta_{ij}$ with $P = 0$ and shear and bulk viscosities $\eta = \frac{1}{2}\frac{1}{1+\nu}$ and $\zeta = \frac{1}{2}\frac{1}{1-\nu}$. After re-interpreting these variables, we can re-use most of the VP-code without additional changes. For details of the discretisation we refer to Plante and others (2020).

On the staggered C-grid, some variables are naturally defined at center (C) points (e.g., σ_{11}), while others are naturally defined at corner (Z) points (e.g., σ_{12} and $\dot{\varepsilon}_{12}$) (Losch and others, 2010). Numerical stability requires that σ_{12}, d_{crit}, d, λ^{-1}, and E are defined on both C- and Z-points of the C-grid cell. The associated averaging is reduced to a minimum, so that only d_{crit}, d, h, a are linearly averaged to Z-points and only $(\dot{\varepsilon}_{12})^2$ is averaged to C-points. E, λ^{-1}, and σ_{12} are computed for center and corner points with the averaged variables.

Validation

We confirmed the plausibility of our MEB implementation with analytic solutions and symmetry tests (not shown, see Chapters 6 and 7 in Bourgett, 2022) and with a reproduction of an idealized ice channel (Plante and others, 2020, not shown).

The general behaviour of the dynamics is identical to previous results (Plante and others, 2020). At the beginning of the simulation the tensile stresses downstream of the channel increase and damage develops downstream of each channel boundary. After 3300 s ($\tau = 0.06\,\mathrm{N\,m^{-2}}$) a concave shape at the downstream end of the channel indicates the ice arching effect. The stress values agree with the previous results (Plante and others, 2020, their Fig. 9). The divergent stress in the middle of the channel is small. The tensile stresses and the shear stresses in the downstream corners of the channel increase so that damage extends over the channel . The ice detaches from the upstream coastline but does not move yet (it remains landfast, land-locked by the islands). Both shear and divergent stress fields downstream of the ice channel drop to zero when the ice downstream of the channel detaches (not shown, see Chapter 7 in Bourgett, 2022).

Table 1. Model parameters of the channel with idealised ice bridge experiment and the quadratic domain with cyclonic winds ("benchmark") for the MEB and the VP rheology.

		channel		"benchmark"		
Parameter	Definition	MEB	VP	MEB	VP	Unit
Δx	Spatial resolution	2		2, 4, 8		km
Δt	Time step	0.5		0.5	120	s
T_d	Damage time	2	-	2	-	s
T_h	Healing time	-	-	1×10^5	-	s
E_0	Elastic modulus	1×10^9	-	5×10^8	-	$\mathrm{N\,m^{-2}}$
P^*	Ice strength	-	27.5	-	27.5	$\mathrm{kN\,m^{-2}}$
ν	Poisson ratio	0.3	-	0.3	-	
λ_0	Relaxation time scale	1×10^5	-	1×10^7	-	s
α	Damage parameter	4	-	4	-	
μ	Internal friction	0.71	-	0.7	-	
c	Cohesion	10, 30, 50	-	1.56, 25	-	$\mathrm{kN\,m^{-2}}$
e	Ellipse aspect ratio	-	1.2, 1.6, 2	-	2	
ρ_a	Air density	1.3		1.3		$\mathrm{m^{-3}}$
ρ_i	Sea ice density	9×10^2		9×10^2		$\mathrm{m^{-3}}$
ρ_w	Water density	1.026×10^3		1.026×10^3		$\mathrm{m^{-3}}$
C_a	Air drag coefficient	1.2×10^{-3}		1.2×10^{-3}		
C_w	Water drag coefficient	5.5×10^{-3}		5.5×10^{-3}		
f_0	Coriolis parameter	0		1.46×10^{-4}		$\mathrm{s^{-1}}$
C^*	Ice concentration parameter	20		20		

COMPARISON OF MEB TO VP

We can now use the MITgcm model framework to compare small-scale sea ice deformations with the VP and the MEB rheology using the same grid spacing, discretization, and parameters.

For both rheologies the yield curve determines the cohesive strength. The cohesive strength influences the shear deformation of sea ice. If sea ice is driven through a narrow channel the cohesive strength controls the potential for modelled sea ice to form ice arches (Ip, 1993; Hibler and others, 2006; Plante and others, 2020).

For the VP and the MEB rheology, cohesive stress states $\sigma_I < |\sigma_{II}|$ are marked by grey shading in Fig. 1. In terms of the mechanical strength parameters for maximal compression, shear and isotropic tension (P, S, T), the ellipse aspect ratio is defined as $e = (P + T)/(2S)$ with $T = kP$ and the tensile factor k (Bouchat and Tremblay, 2017; König Beatty and Holland, 2010). For the elliptic yield curve, the cohesion increases by decreasing the ratio e of the two semi-major axes (making the ellipse "fatter"), by increasing P, and by moving or extending the ellipse into the tensile half-plane ($k > 0$). Even though the original VP yield curve does not allow isotropic tensile stresses ($T = 0$ or $k = 0$, black ellipse in Fig. 1), the tensile strength is not zero. The maximum tensile stress, that is the maximal distance of the yield curve to the diagonal $\sigma_I = \sigma_{II}$ or maximum of σ_1 (Bouchat and Tremblay, 2017, and Fig. 1), is defined as

$$T_m = \tfrac{1}{2}\left\{(1+k)\sqrt{1+e^{-2}} - (1-k)\right\} P \tag{6}$$

and is non-zero for all $k \geq 0$ (Fig. 1).

We use an idealized ice channel to tune yield curve parameters of both rheologies to give similar results. Building on this experience, we analyse the effect of grid-scale heterogeneity on the solution in a quadratic domain with cyclonic winds (Mehlmann and others, 2021) with similar cohesion for VP and MEB. The VP models uses a JFNK solver that converges with a relative precision of 10^{-4}. All model parameters are summarized in Tabel 1.

Channel with idealised ice bridge

Inspired by previous ice arch simulations (Dumont and others, 2009; Dansereau and others, 2017), we use an idealized channel set-up modified from Plante and others (2020). A 800 km by 200 km domain with a grid resolution of 2 km and closed boundaries with a no-slip boundary condition in the x-direction features a channel in the y-direction. The channel itself is 200 km long and 60 km wide. The domain has open boundaries at $y = 0$ km and $y = 800$ km with Neumann conditions for all variables. The Neumann conditions ensure that sea ice can drift freely into and out of the domain and does not need to detach from a solid boundary at $y = 800$ km, so that slowing down of the ice upstream the channel is solely determined by the ice arching. The sea ice cover is forced by surface stress in the negative y-direction ("southwards") that increases linearly from 0 to $0.625\,\mathrm{N\,m^{-2}}$ within 10 h. The simulation is run for 240 h with no further increase of the forcing. The slowing down of the sea ice upstream of the channel due to the formation of ice arches is used for comparison between VP and MEB.

Different parameters of the yield curves were tested to allow cohesive stress states. We choose the parameters so that the maximum tensile stress T_m (6) of the VP rheology is equal to the critical tensile stress σ_t (4) of the MEB rheology, since both represent the maximum positive value of the principal stress σ_1 (Fig. 1). Specifically, we choose $c = 10\,\mathrm{kN\,m^{-2}}$ and $30\,\mathrm{kN\,m^{-2}}$ leading to $\sigma_t = 10.4\,\mathrm{kN\,m^{-1}}$ and $31.24\,\mathrm{kN\,m^{-1}}$ for MEB. The corresponding T_m are computed with $P^* = 49.92\,\mathrm{kN\,m^{-2}}$ and $P^* = 149.92\,\mathrm{kN\,m^{-2}}$, $k = 0.05$, and a small value for $e = 1.2$ (Kubat and others, 2006; Lemieux and others, 2016).

Except for the VP simulations with $T_m = 31.24\,\mathrm{kN\,m^{-1}}$, the effect of ice arching to the upstream ice drift velocities can be observed and the ice slows down for both VP and MEB simulation (Fig. 2). The parameter set with $T_m = 31.24\,\mathrm{kN\,m^{-1}}$ makes the ice so stiff that it does not start to move at all. The ice drift in the MEB simulation with $c = 30\,\mathrm{kN\,m^{-2}}$ decreases within 40 h. For $10\,\mathrm{kN\,m^{-2}}$, the ice drift upstream increases quickly and then slows down gradually with rates that are very similar between the MEB ($m_{\mathrm{meb}} = 1.45 \times 10^{-7}\,\mathrm{m\,s^{-2}}$) and VP simulations ($m_{\mathrm{vp}} = 1.43 \times 10^{-7}\,\mathrm{m\,s^{-2}}$) (Fig. 2, solid lines). Also, the velocity fields upstream (Fig. 2, Fig. 3) are very similar with $c = 10\,\mathrm{kN\,m^{-2}}$ for MEB and its correspondent mechanical parameters for VP. The maximum "southward" velocity upstream is reached after approximately 15 h.

The effective ice thickness is generally similar for both rheologies (Fig. 3). In both cases, leads form downstream of the channel and ridging occurs upstream of the channel. Some differences in the exact location and shape of the leads and ridges are attributed to the different failure processes, namely the damage propagation and the associated normal flow rule for the MEB and VP rheologies, respectively. For instance, some ice remains attached to the islands downstream of the channel in the VP simulation as the deformation transitions from lead opening downstream of the islands to pure shear on the sides, while in

[t]

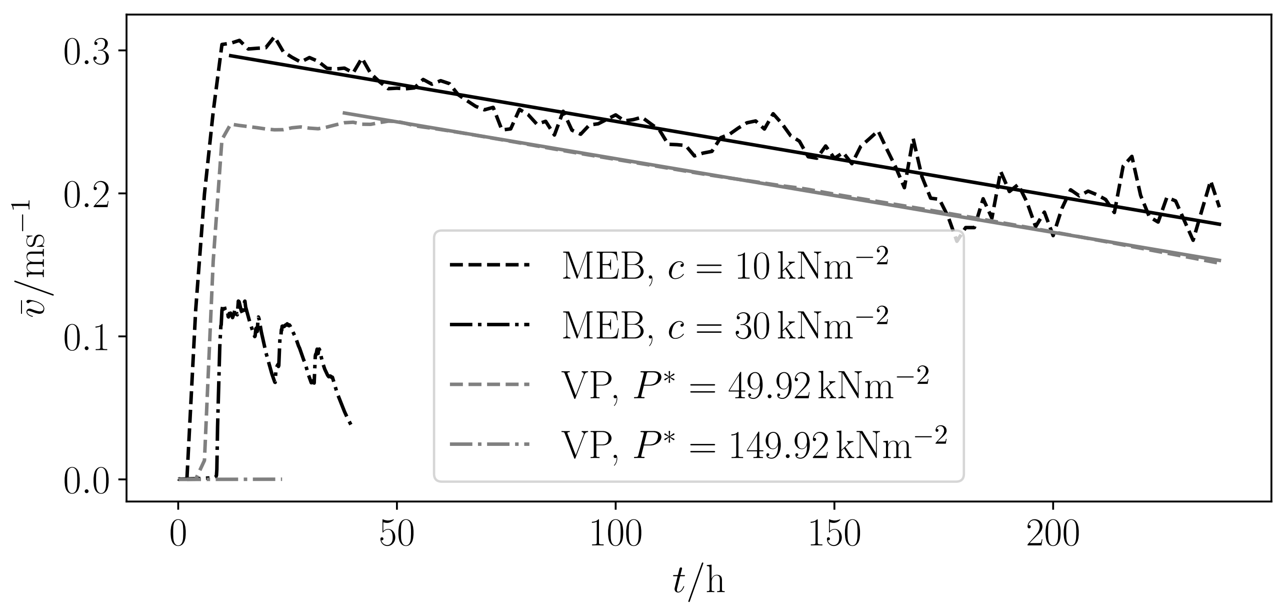

Fig. 2. Averaged ice velocities parallel to channel upstream of channel. The sea ice does not move at all (VP) or rapidly stops (MEB) for the high cohesion case ($c = 30\,\mathrm{kN\,m}^{-2}$, $P^* = 149.92\,\mathrm{kN\,m}^{-2}$, dash-dotted lines). There is a slow and very similar stopping effect by the formation of an ice arch in both the MEB simulation and the VP simulation for the low cohesion case ($c = 10\,\mathrm{kN\,m}^{-2}$, $P^* = 49.92\,\mathrm{kN\,m}^{-2}$, dashed lines). The solid lines are the linear regression of the ice velocities.

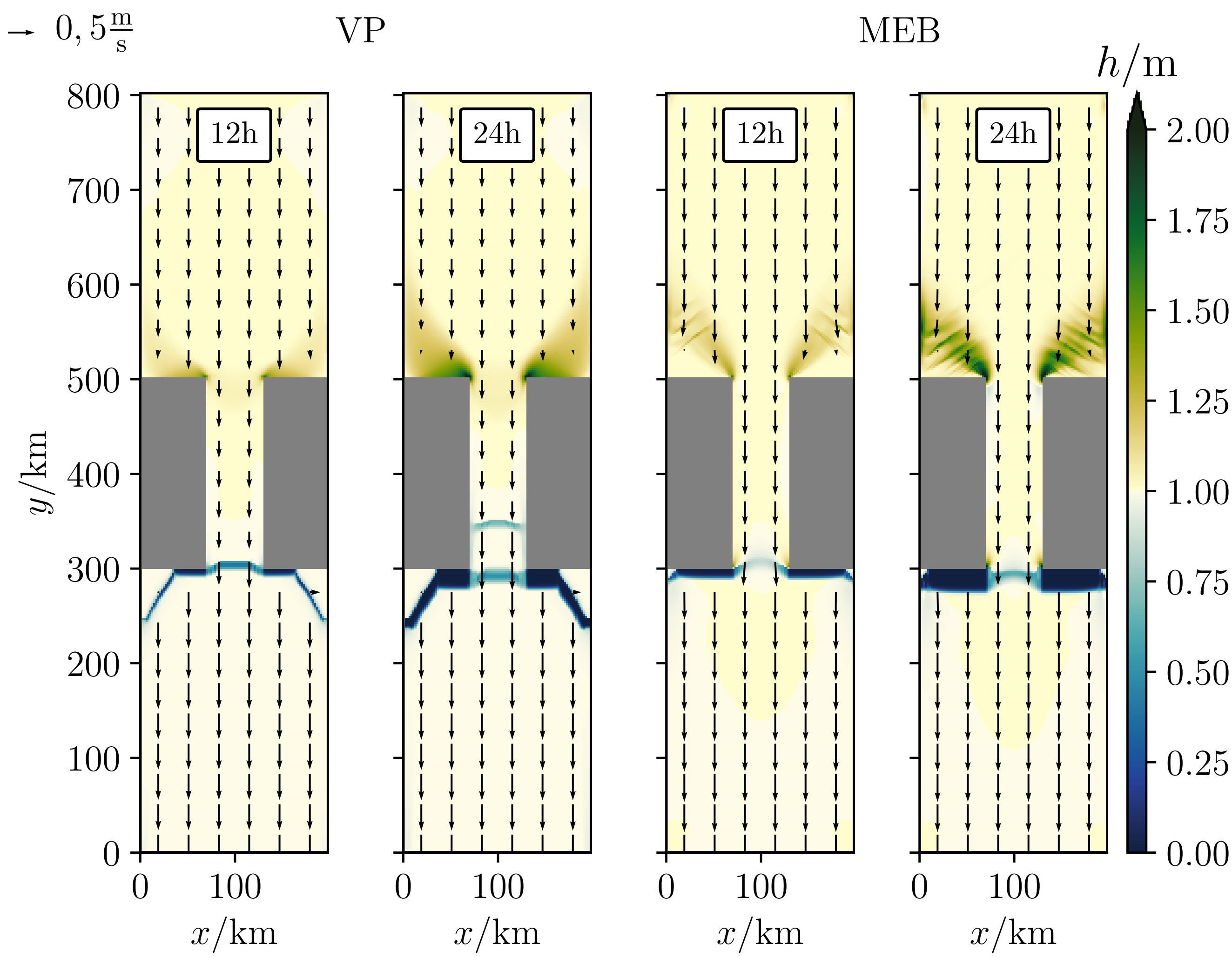

Fig. 3. Snapshots of the effective ice thickness h and the ice drift velocity (arrows) for the VP rheology (left two panels) and the MEB rheology (right two panels) at $t = 12\,\text{h}$ and $24\,\text{h}$. Note that the colour scale is chosen to emphasize deviations from the initial state ($h = 1\,\text{m}$).

the MEB simulation the damage propagation is directly along the coastlines. Upstream of the channel, the ridging area contains additional diagonal patterns in the MEB simulations due to the formation of secondary fracture lines, while the ice thickness is smoother and more uniform in the VP simulations.

Our results agree with other ice arch simulations (Dumont and others, 2009; Dansereau and others, 2017; Plante, 2021, Chapter 5) and demonstrate that the cohesive strength of the ice plays an important role in ice arching so that corresponding mechanical parameters lead to similar results between the different rheologies.

Quadratic domain with cyclonic winds

A quadratic box with closed boundaries, constant anticyclonic (clockwise) ocean circulation and a moving cyclonic wind system was suggested to compare different sea ice models (Mehlmann and others, 2021). This "benchmark" problem was used to analyse how different VP models simulate sea ice deformation, in particular LKFs. Here, the "benchmark" problem is repeated with the MITgcm using different grid spacings (Δx =2, 4, 8 km) to analyse spatial heterogeneity in both the MEB and VP models. Note that for all grid resolutions the simulation is produced with the same time step ($\Delta t = 120\,\mathrm{s}$ for VP, $\Delta t = 0.5\,\mathrm{s}$ for MEB). In the MEB case, this value is chosen to ensure that the constitutive equation is well resolved at the highest resolution (i.e., according to the CFL criterion for resolving the elastic waves). If we want to choose analagous yield curve parameters for MEB and VP as in the channel experiment, we have to consider the following: The VP-parameters of this benchmark $P^* = 27.5\,\mathrm{kN/m^2}$ with $e = 2$ and no tensile stress ($k = 0$) lead to a very low cohesion of $1.56\,\mathrm{kN\,m^2}$ (Eq. 6). Using the large P^* values implied by the cohesion of the channel experiment in the VP rheology would change the benchmark dramatically from previously published results (Mehlmann and others, 2021), so that to compare the different rheologies we instead adjust the MEB parameters to match the low VP cohesion. The low cohesion of $1.56\,\mathrm{kN\,m^2}$ leads to very low stress states. For comparison, we also use a high value of $c = 25\,\mathrm{kN\,m^2}$. These cohesion values cover the range of previously reported values (Plante and others, 2020; Dansereau and others, 2016). The model parameters for the experiments are summarized in Table 1.

Results from Mehlmann and others (2021) are reproduced exactly by our VP simulations, with more radial features in the compressive stress field than circular ones and without tensile stress states (Fig. 4). In both models, there are fewer identifiable deformation patterns and the deformation fields also become smoother with decreasing resolution (not shown, see Chapter 8 in Bourgett, 2022).

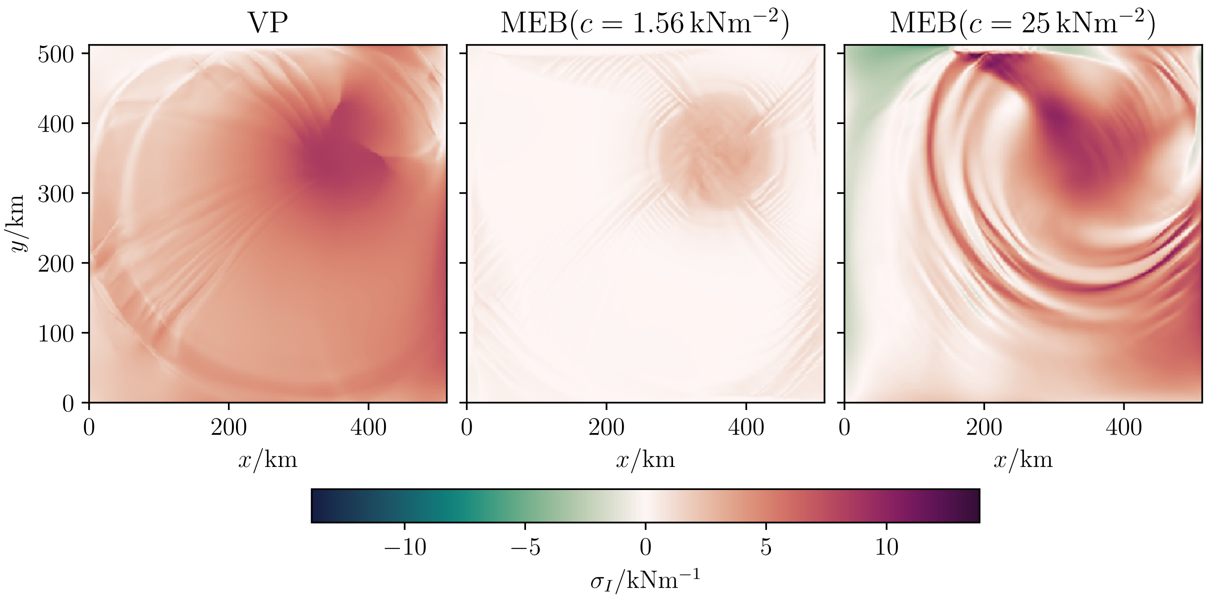

Fig. 4. Snapshot of the stress invariant σ_I at $t = 2\,\mathrm{d}$ and with $\Delta x = 2\,\mathrm{km}$ of the VP simulation on the left and the MEB rheology with low (center) and high (right) cohesion. Positvite values mean convergence. Divergent (negative) stress state are only allowed in the MEB-model. The size of the stress invariant depends on the choice of the cohesion.

The presence of radial or circular features and the range of the stress values depends to some degree on the choice of cohesion for the MEB rheology. Using the MEB rheology with a cohesion similar to that of the VP simulations yields much smaller stresses but otherwise similar features as in the VP simulations, with mostly radial features and only a few circular stress features. Increasing the cohesion in the MEB model to get similar stress states as in the VP simulation (Fig. 4), however, changes these patterns and the features are mostly circular. Using the VP rheology with analogous values to match the cohesive stress states results in the same dependency (not shown). This dependency suggests that the shape of the features are sensitive to the shear strength; fewer cohesive stress states (gray area in Fig. 1) strongly result in smaller shear stresses which favor radial features, while more cohesive stress states result in larger shear stresses which favor the production of circular features.

Differences in the stress fields could also be influenced by the different yield curve shape: the MEB rheology allows isotropic tensile stresses (see negative σ_I in Fig. 4), while the VP rheology with the standard elliptical yield curve does not. In addition, the MEB model does not have a flow rule.

Further, the rheologies are compared by means of the number of LKFs as detected by a tracking algorithm (Hutter and Losch, 2020, with parameter modifications by Mehlmann and others, 2021) (Table 2). The number of LKFs increases for both rheologies with increasing resolution. As expected because of the

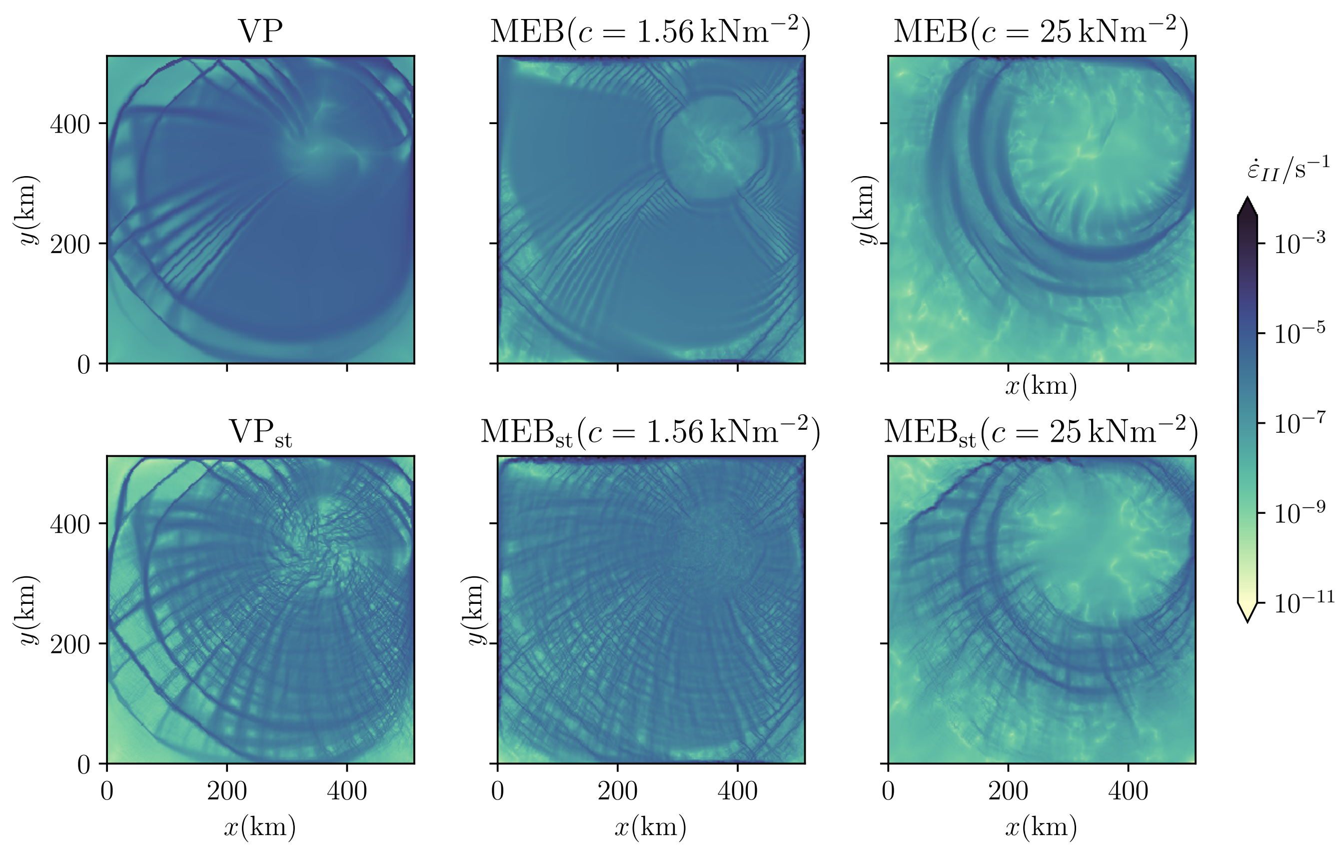

Fig. 5. Snapshots of the shear deformation rate $\dot{\varepsilon}_{II}$ at $t = 2\,\mathrm{d}$ and with $\Delta x = 2\,\mathrm{km}$ of simulations without (above) and with (below) a stochastic pramaterisation of the heterogeneity at the grid-scale (index "st"). The shear deformation rate using the VP rheology on the left and using the MEB rheology with low and high cohesion in the center and on the right.

damage mechanism and long-range elastic interactions that produce sub-grid fracturing (Dansereau and others, 2016), the MEB simulation (independent of the choice of cohesion) has more LKFs than the VP simulation on all grids, especially on $\Delta x = 2\,\mathrm{km}$ grid. Increasing the cohesion tends to lead to fewer LKFs (Table 2). Note that the decreased heterogeneity in the MEB simulations with high cohesion is associated with a much less extensive damage field. As the damage mechanism is known to be a numerical error integrator (Plante and Tremblay, 2021), this raises a question about the impact of numerical noise in seeding the heterogeneity.

STOCHASTIC PARAMETERISATION

One of the main motivations to develop a brittle rheology was the observation that models with VP rheology underestimate observed spatial heterogeneity (Girard and others, 2011). We indeed found the MEB solution

Table 2. Number of LKFs for both VP and MEB rheology for simulations with 2 km, 4 km, and 8 km grid spacing Δx. The index "st" indicates that the simulation uses a stochastic parameterisation of c (cohesion) for the MEB rheoogy or P^* (ice strength) for the VP rheology. The MEB simulations are run with a high value of $c = 25\,\mathrm{kN\,m^2}$ and with a low value of $c = 1.56\,\mathrm{kN\,m^2}$

	Grid resolution Δx		
	2 km	4 km	8 km
MEB ($c = 25\,\mathrm{kNm^{-2}}$)	128	51	21
$\mathrm{MEB_{st}}$ ($c = 25\,\mathrm{kNm^{-2}}$)	241	76	23
MEB ($c = 1.56\,\mathrm{kNm^{-2}}$)	143	52	15
$\mathrm{MEB_{st}}$ ($c = 1.56\,\mathrm{kNm^{-2}}$)	390	89	21
VP	51	31	7
$\mathrm{VP_{st}}$	317	106	30

to be more heterogeneous. Alternatively, heterogeneity can be increased with stochastic parameterisations (Juricke and others, 2013, their Fig. 6, and personal communication). In fact, early brittle models used a stochastic cohesion parameter c to introduce disorder (Girard and others, 2011; Dansereau and others, 2017). We now adopt the same method to account for faults and cracks in the ice below the spatial grid scale Δx and draw the cohesion parameter c from a (pseudo-)random uniform distribution between $0.5c_0$ and $1.5c_0$ of the unperturbed cohesion c_0. The resulting heterogeneous cohesion field is constant in time throughout the simulation. Because the critical stresses σ_c and σ_t depend on c (Eqs. 3 and 4), a stochastic cohesion also leads to a different (but constant-in-time) damage criterion for each grid cell.

With the stochastic cohesion the number of LKFs increases for all grid resolutions independent of the cohesion (Table 2). The number of LKFs for the MEB simulations with the stochastic cohesion is also much higher than for the VP simulations discussed above (consistent with Girard and others, 2011).

Can we also obtain more spatial heterogeneity with stochastic parameters within the VP model? The VP model does not contain the fast feedback caused by the damage parameter, but the ice strength P^* can be perturbed by drawing from the same (pseudo-)random field as the cohesion in the MEB rheology, such that the elliptic yield curve is enlarged or reduced for each grid cell according to $P^{*'} \in [0.5P^*, 1.5P^*]$. This choice of P^* increases the number of LKFs in all resolutions (Table 2). The LKF numbers are comparable to the corresponding MEB numbers and even higher for lower resolutions.

In both rheologies, heterogeneity of the results can be increased by introducing spatial variability to mechanical ice properties (c, P^*). The simulations (e.g., shear deformation rate, Fig. 5) contain features of heterogeneity that appear similar to previous results (Girard and others, 2011, their Fig. 3b). We find (Table 2) that a VP model with a stochastic parameterisation can have a similar spatial heterogeneity as the MEB rheology. Note, that here a random perturbation of mechanical parameters was similar in both rheologies, whereas Girard and others (2011) compared a standard VP model with smooth ice strength to an EB model with stochastic cohesion. We also note, that this random perturbation of cohesion is generally not used in realistic large scale MEB or BBM simulations with realistic domains (e.g., Rampal and others, 2016; Olason and others, 2022)

CONCLUSION

Simulations with the MEB rheology tend to be more heterogeneous (i.e., have more linear kinematic features) than simulations with the standard VP rheology. This result was anticipated, but shown here in a controlled environment without confounders. Furthermore, we demonstrate that adding disorder by stochastic mechanical parameters (cohesion for MEB, ice strength for VP) increases heterogeneity to similar levels in the VP and MEB simulations. We conclude that grid-scale heterogeneity is one important driver to produce prominent large-scale deformation features, such as LKFs. Grid-scale heterogeneity can be introduced in various ways, for example, by a brittle rheology based on physical considerations or by local modification (physical or statistical) of material properties. The latter can be applied to sea ice models independent of the constitutive equation.

After identifying the most important material properties (here: cohesion in a landfast ice simulation in a channel), these can be chosen in such a way that simulations with MEB and VP rheology lead to very similar deformation fields. With the cohesion chosen to be similar, the stress states are very different in magnitude between VP and MEB. In contrast, tuning the stress states to be of similar order of magnitude makes the deformations very different. In this sense, our results suggest that the choice of constitutive equation (MEB or VP) has a smaller effect on the deformation patterns than tuning the respective yield curves.

There is some structural similarity between the constitutive equations for VP and MEB such that after re-interpretation of some variables, a large part of the VP code can be used for the implementation of the MEB rheology (Plante and others, 2020). The time-derivative term, however, increases error memory in the system (Plante and Tremblay, 2021). Numerical details, such as averaging between center and corner points of the C-grid, prove to be crucial for stability of the MEB implementation. The new damage equation and in particular the elastic wave propagation further pose strict constraints on the time step, so that a time splitting method for the MEB code should be used (Olason and others, 2022).

In our simulations, disorder introduced by noise (stochastic parameters) seems to be an important driver of heterogeneity. The VP simulations without additional noise in the ice strength have much fewer LKFs than those with a stochastic strength parameter. The same is true for the MEB simulations but to a smaller extend. Whether the integration of numerical errors by the damage parameter plays a role remains to be determined. We speculate that using a stabilizing scheme for stress correction that minimizes the numerical errors (Plante and Tremblay, 2021) will reduce the simulated heterogeneity.

REFERENCES

Berner J, Achatz U, Batte L, Bengtsson L, De La Camara A, Christensen HM, Colangeli M, Coleman DR, Crommelin D, Dolaptchiev SI and others (2017) Stochastic parameterization: Toward a new view of weather and climate models. *Bulletin of the American Meteorological Society*, **98**(3), 565–588

Bouchat A and Tremblay B (2017) Using sea-ice deformation fields to constrain the mechanical strength parameters of geophysical sea ice. *Journal of Geophysical Research: Oceans*, **122**(7), 5802–5825

Bouchat A, Hutter NC, Dupont JCF, Dukhovskoy DS, Garric G, Lee YJ, Lemieux JF, Lique C, Losch M, Maslowski W, Myers PG, Ólason E, Rampal P, Rasmussen T, Talandier C, Tremblay B and Wang Q (2022) Sea Ice Rheology Experiment (SIREx), Part I: Scaling and statistical properties of sea-ice deformation fields. *J. Geophys. Res.*, **127**(4), e2021JC01766 (doi: 10.1029/2021JC017667)

Bourgett M (2022) *Implementation of a Maxwell Elasto-Brittle Rheology in a Sea Ice Model Coupled to an Ocean*. Master's thesis, TU Dortmund, Dortmund, GER, `http://hdl.handle.net/10013/epic.febd7a61-c2cf-4f4f-b86d-76beaf2d4378`

Boutin G, Ólason E, Rampal P, Regan H, Lique C, Talandier C, Brodeau L and Ricker R (2023) Arctic sea ice mass balance in a new coupled ice–ocean model using a brittle rheology framework. *The Cryosphere*, **17**(2), 617–638

Danilov S, Sidorenko D, Wang Q and Jung T (2017) The Finite-volumE Sea ice–Ocean model (FESOM2). *Geoscientific Model Development*, **10**(2), 765–789

Dansereau V, Weiss J, Saramito P and Lattes P (2016) A Maxwell elasto-brittle rheology for sea ice modelling. *The Cryosphere*, **10**(3), 1339–1359

Dansereau V, Weiss J, Saramito P, Lattes P and Coche E (2017) Ice bridges and ridges in the Maxwell-EB sea ice rheology. *The Cryosphere*, **11**(5), 2033–2058

Dumont D, Gratton Y and Arbetter TE (2009) Modeling the dynamics of the North Water polynya ice bridge. *Journal of Physical Oceanography*, **39**(6), 1448–1461

Girard L, Bouillon S, Weiss J, Amitrano D, Fichefet T and Legat V (2011) A new modeling framework for sea-ice mechanics based on elasto-brittle rheology. *Annals of Glaciology*, **52**(57), 123–132

Hibler W, Hutchings J and Ip C (2006) Sea-ice arching and multiple flow states of Arctic pack ice. *Annals of Glaciology*, **44**, 339–344

Hibler WD III (1979) A dynamic thermodynamic sea ice model. *J. Phys. Oceanogr.*, **9**(4), 815–846

Hunke EC and Dukowicz JK (1997) An elastic–viscous–plastic model for sea ice dynamics. *Journal of Physical Oceanography*, **27**(9), 1849–1867

Hutter N and Losch M (2020) Feature-based comparison of sea ice deformation in lead-permitting sea ice simulations. *The Cryosphere*, **14**(1), 93–113

Hutter NC, Bouchat A, Dupont F, Dukhovskoy DS, Koldunov NV, Lee YJ, Lemieux JF, Lique C, Losch M, Maslowski W, Myers PG, Ólason E, Rampal P, Rasmussen T, Talandier C, Tremblay B and Wang Q (2022) Sea Ice Rheology Experiment (SIREx), Part II: Evaluating simulated linear kinematic features in high-resolution sea-ice simulations. *J. Geophys. Res.*, **127**(4), e2021JC017666 (doi: 10.1029/2021JC017666)

Ip CF (1993) *Numerical investigation of different rheologies on sea-ice dynamics*. Dartmouth College

Juricke S, Lemke P, Timmermann R and Rackow T (2013) Effects of stochastic ice strength perturbation on Arctic finite element sea ice modeling. *Journal of climate*, **26**(11), 3785–3802

Kimmritz M, Danilov S and Losch M (2016) The adaptive EVP method for solving the sea ice momentum equation. *Ocean Modelling*, **101**, 59–67

König Beatty C and Holland DM (2010) Modeling landfast sea ice by adding tensile strength. *J. Phys. Oceanogr.*, **40**(1), 185–198 (doi: 10.1175/2009JPO4105.1)

Kubat I, Sayed M, Savage S and Carrieres T (2006) Flow of ice through converging channels. *International Journal of Offshore and Polar Engineering*, **16**(04)

Lemieux JF, Tremblay B, Thomas S, Sedláček J and Mysak LA (2008) Using the preconditioned Generalized Minimum RESidual (GMRES) method to solve the sea-ice momentum equation. *J. Geophys. Res.*, **113**(C10004) (doi: 10.1029/2007JC004680)

Lemieux JF, Tremblay B, Sedláček J, Tupper P, Thomas S, Huard D and Auclair JP (2010) Improving the numerical convergence of viscous-plastic sea ice models with the Jacobian-free Newton-Krylov method. *J. Comp. Phys.*, **229**, 2840–2852 (doi: 10.1016/j.jcp.2009.12.011c)

Lemieux JF, Dupont F, Blain P, Roy F, Smith GC and Flato GM (2016) Improving the simulation of landfast ice by combining tensile strength and a parameterization for grounded ridges. *Journal of Geophysical Research: Oceans*, **121**(10), 7354–7368

Losch M and Danilov S (2012) On solving the momentum equations of dynamic sea ice models with implicit solvers and the Elastic Viscous-Plastic technique. *Ocean Modelling*, **41**, 42–52 (doi: 10.1016/j.ocemod.2011.10.002)

Losch M, Menemenlis D, Campin JM, Heimbach P and Hill C (2010) On the formulation of sea-ice models. part 1: Effects of different solver implementations and parameterizations. *Ocean Modelling*, **33**(1-2), 129–144

Losch M, Fuchs A, Lemieux JF and Vanselow A (2014) A parallel Jacobian-free Newton-Krylov solver for a coupled sea ice-ocean model. *J. Comp. Phys.*, **257**(A), 901–910, ISSN 0021-9991 (doi: 10.1016/j.jcp.2013.09.026)

Marshall J, Adcroft A, Hill C, Perelman L and Heisey C (1997) A finite-volume, incompressible Navier Stokes model for studies of the ocean on parallel computers. *J. Geophys. Res.*, **102**(C3), 5753–5766 (doi: 10.1029/96JC02775)

Mehlmann C, Danilov S, Losch M, Lemieux JF, Hutter N, Richter T, Blain P, Hunke E and Korn P (2021) Simulating linear kinematic features in viscous-plastic sea ice models on quadrilateral and triangular grids with different variable staggering. *Journal of Advances in Modeling Earth Systems*, **13**(11), e2021MS002523

MITgcm Group (2021) MITgcm User Manual. Online documentation, MIT/EAPS, Cambridge, MA 02139, USA (doi: 10.5281/zenodo.1409237), `https://mitgcm.readthedocs.io/en/latest`

Olason E, Boutin G, Korosov A, Rampal P, Williams T, Kimmritz M, Dansereau V and Samaké A (2022) A new brittle rheology and numerical framework for large-scale sea-ice models. *Journal of Advances in Modeling Earth Systems*, **14**(8), e2021MS002685

Plante M (2021) *A generalized damage parameterization within the Maxwell Elasto-Brittle rheology: applications to ice fractures and ice arches in landfast ice simulations.* Phd thesis, McGill University, https://escholarship.mcgill.ca/concern/theses/gf06g703w

Plante M and Tremblay LB (2021) A generalized stress correction scheme for the Maxwell elasto-brittle rheology: impact on the fracture angles and deformations. *The Cryosphere*, **15**(12), 5623–5638

Plante M, Tremblay LB, Losch M and Lemieux JF (2020) Landfast sea ice material properties derived from ice bridge simulations using the Maxwell elasto-brittle rheology. *The Cryosphere*, **14**(6), 2137–2157

Rampal P, Bouillon S, Ólason E and Morlighem M (2016) neXtSIM: a new Lagrangian sea ice model. *The Cryosphere*, **10**(3), 1055–1073

Ringeisen D, Losch M, Tremblay LB and Hutter N (2019) Simulating intersection angles between conjugate faults in sea ice with different viscous–plastic rheologies. *The Cryosphere*, **13**(4), 1167–1186

Ringeisen D, Tremblay LB and Losch M (2021) Non-normal flow rules affect fracture angles in sea ice viscous–plastic rheologies. *The Cryosphere*, **15**(6), 2873–2888

Ringeisen D, Losch M and Tremblay LB (2023) Teardrop and parabolic lens yield curves for viscous-plastic sea ice models: New constitutive equations and failure angles. *Journal of Advances in Modeling Earth Systems*, **15**(9), e2023MS003613 (doi: https://doi.org/10.1029/2023MS003613)

Sodhi DS (1977) Ice arching and the drift of pack ice through restricted channels. Technical Report 77–18, Department of Defense, Department of the Army, Corps of Engineers, Cold Regions Research and Engineering Laboratory, Hanover, New Hampshire

Turner AK, Lipscomb WH, Hunke EC, Jacobsen DW, Jeffery N, Engwirda D, Ringler TD and Wolfe JD (2022) MPAS-Seaice (v1.0.0): sea-ice dynamics on unstructured Voronoi meshes. *Geoscientific Model Development*, **15**(9), 3721–3751 (doi: 10.5194/gmd-15-3721-2022)

Walker D (1966) An approximate theory for pressures and arching in hoppers. *Chemical Engineering Science*, **21**(11), 975–997

Weiss J, Schulson EM and Stern HL (2007) Sea ice rheology from in-situ, satellite and laboratory observations: Fracture and friction. *Earth and Planetary Science Letters*, **255**(1-2), 1–8